




## Local phase transformations during current-induced forming and degradation in TiN/HfO<sub>2</sub>/Pt metal/oxide/metal heterostructures

 Aikerul Ece\*

School of Applied Sciences, Beykent University, Istanbul, Turkey

\*Correspondence: [aikerece@tutamail.com](mailto:aikerece@tutamail.com)

**Abstract.** This work investigates how current-induced forming and electrical stressing give rise to local structural and compositional transformations in TiN/HfO<sub>2</sub>/Pt metal/oxide/metal devices used as model resistive memory cells. TiN/HfO<sub>2</sub>/Pt structures with an approximately nine-nanometre-thick atomic-layer-deposited HfO<sub>2</sub> layer and device diameters of 5–20 micrometres were fabricated using CMOS-compatible processes. Electrical current–voltage and conductance–current characteristics were combined with in situ X-ray diffraction under bias and ex situ focused-ion-beam-prepared transmission electron microscopy and scanning electron microscopy, including energy-dispersive X-ray spectroscopy, on devices with well-documented electrical histories. Pristine devices showed uniform, area-scaled leakage currents of a few tens of nanoamperes at 0.1 volt, indicating a structurally homogeneous oxide. Electrical forming occurred reproducibly at about 2.5–3.0 volts with current compliance in the 100–500 microampere range and produced low-resistance states with conductance of approximately 2–3 millisiemens. With increasing cycle number and stronger current stressing, low-resistance conductance increased in a statistically significant way, while parts of the conductance–current curves became irreversible. In situ X-ray diffraction revealed the emergence of weak additional diffraction features attributed to transformed hafnium oxide only after strong current loading, while the metal electrodes remained largely unchanged. Cross-sectional microscopy showed that these electrical changes correlate with the appearance of localized filament-like regions, oxygen-deficient zones and mild interfacial reactions near the top electrode. Taken together, these observations establish a direct correlation between electrical forming and degradation regimes and spatially confined structural transformations within the HfO<sub>2</sub> layer and at metal/oxide interfaces. This understanding provides a basis for engineering more reliable resistive memory devices by defining electrical stress windows that avoid the onset of irreversible structural changes.

**Keywords:** metal/oxide/metal heterostructures, electrical forming and degradation, local phase transformations, HfO<sub>2</sub>-based resistive switching, filamentary conduction.

### 1. Introduction

Metal/oxide/metal (MOM) heterostructures are a central platform for modern non-volatile memories, neuromorphic computing elements, and compact selectors, because they exhibit electric-field-induced resistive switching and controllable soft breakdown phenomena [1]. In such devices, information is encoded in the conductance of a thin insulating or semiconducting oxide layer, which can be reversibly switched between high- and low-resistance states by voltage or current pulses through the formation and rupture of localized conductive paths. These effects underlie a broad class of resistive random access memories (RRAM) based on transition-metal oxides such as HfO<sub>2</sub>, Al<sub>2</sub>O<sub>3</sub>, and TiO<sub>2</sub>, where switching is typically governed by nanoscale rearrangement of oxygen vacancies, cation motion, and local redox reactions within the oxide and at its interfaces with metallic electrodes [2], [3], [4]. Understanding how these point defects couple to structural transformations and local phase changes under current stressing remains a key challenge for improving device stability and scalability.

Hafnium oxide is a key dielectric in resistive switching cells due to its compatibility with CMOS processes and its rich defect chemistry. Numerous studies have shown that switching in HfO<sub>2</sub>-based stacks is associated with oxygen-vacancy-rich filaments connecting the two electrodes, formed during an initial soft-breakdown-like “electrical forming” step and subsequently modified during set/reset cycling. Device-level measurements on Ni/HfO<sub>2</sub>/Pt and related stacks have revealed large ON/OFF ratios, good retention, but also pronounced variability of forming and switching voltages attributed to stochastic filament nucleation and growth [5], [6]. Complementary microscopy work has directly imaged conductive filaments in HfO<sub>2</sub> memories, showing conical or multi-filament morphologies and strong localization of current flow [7], [8]. These observations indicate that local microstructure, including grain boundaries and amorphous–crystalline interfaces, plays a decisive role in defining where soft breakdown initiates and how it propagates within the oxide layer.

Recent in situ and operando studies have started to bridge the gap between electrical characteristics and the underlying nanoscale structural evolution. In situ TEM investigations of HfO<sub>2</sub>-based RRAM have visualized the gradual build-up and dissolution of nanofilaments under bias, linking oxygen-vacancy redistribution and local changes in phase contrast to the SET and RESET processes [9]. Similar in situ TEM/EDS work on HfO<sub>2</sub>/Al<sub>2</sub>O<sub>3</sub> bilayers has demonstrated that current stressing can drive extended defect formation at internal interfaces and even cation migration from metal electrodes into the oxide stack, ultimately leading to degraded resetability and failure [10]. Operando hard X-ray photoelectron spectroscopy has revealed reversible modulation of interfacial oxidation states—so-called “oxygen breathing”—during resistive switching, underscoring the dynamic character of local chemistry under electrical load [11]. Together, these studies show that the resistive state of an MOM cell is not only a function of the filament core but also of its surrounding matrix and interfaces, where subtle phase and stoichiometry changes accumulate over time.

Another crucial ingredient is microstructural engineering of the oxide layer itself. Grain-boundary-engineered HfO<sub>2</sub> films have been shown to support forming-free RRAM operation, where pre-designed low-energy grain boundaries act as preferred breakdown paths and significantly reduce device-to-device variation [12]. More recently, systematic control of grain boundary density and orientation in polycrystalline HfO<sub>2</sub> has been correlated with improved endurance and narrower distributions of switching parameters, highlighting the importance of extended defects in determining failure modes and long-term reliability [13]. In parallel, compositional and defect-engineering strategies have focused on tuning the concentration and distribution of oxygen vacancies in HfO<sub>2-x</sub> films, demonstrating that vacancy-rich profiles can lower forming voltages but may also enhance variability and accelerate degradation under repeated cycling [14], [15].

Despite these extensive efforts, most structural studies either focus on isolated nanoscale regions under highly specific bias conditions, or on fully failed devices, while many electrical studies treat the oxide and interfaces as fixed backgrounds whose microstructure is only qualitatively inferred. As a result, there is still a lack of device-scale, statistically supported correlations that link well-defined electrical stress histories—pristine, formed, moderately cycled, and heavily stressed states—to directly observed structural and compositional changes in technologically relevant TiN/HfO<sub>2</sub>/Pt stacks. In particular, it remains unclear to what extent different conductance regimes correspond to (i) relatively benign rearrangements of oxygen vacancies within an amorphous matrix, or (ii) more substantial transformations such as local crystallization of HfO<sub>2</sub>, formation of substoichiometric HfO<sub>x</sub> phases, and interfacial reactions with the electrodes.

The working hypothesis of this study is that in TiN/HfO<sub>2</sub>/Pt metal/oxide/metal devices, electrical forming and subsequent current stressing drive a sequence of spatially confined structural transformations in both the HfO<sub>2</sub> layer and the adjacent electrodes, and that these transformations correlate systematically with the observed evolution of low-resistance conductance and degradation behaviour. We specifically assume that an initially homogeneous amorphous oxide develops localized oxygen-deficient regions and, under stronger stress, partially crystallized HfO<sub>x</sub>-like domains along preferred microstructural pathways, and that these changes can be detected as subtle modifications of diffraction patterns and as filament-like contrast with altered local chemistry in cross-sectional electron microscopy.

The goal of the present work is therefore to establish quantitative correlations between electrical history, local phase composition, and microstructural evolution in TiN/HfO<sub>2</sub>/Pt metal/oxide/metal heterostructures under controlled current loading. To this end, we combine statistical current–voltage and conductance–current measurements on ensembles of devices with in situ X-ray diffraction during biasing and ex situ focused-ion-beam-based transmission electron microscopy, scanning electron microscopy and energy-dispersive X-ray spectroscopy on selected cells that represent distinct electrical states. By analysing these datasets together, we seek to identify characteristic structural signatures of different forming and degradation regimes and to provide experimentally grounded guidelines for defining safe operating windows that avoid irreversible local transformations in HfO<sub>2</sub>-based resistive memories.

## 2. Methods

### 2.1. Materials and device fabrication

Metal/oxide/metal (MOM) heterostructures were fabricated on 100 mm Si(100) wafers with a thermally grown SiO<sub>2</sub> layer (~200 nm). The bottom electrode (BE) consisted of a Ti (10 nm) adhesion layer and a Pt (100 nm) layer deposited by DC magnetron sputtering at room temperature in Ar atmosphere. The wafer was then patterned by standard photolithography and ion-beam etching to define square BE pads (100 × 100 μm<sup>2</sup>).

The resistive switching layer was a HfO<sub>2</sub> film with a thickness of 8–10 nm deposited by thermal atomic layer deposition (ALD) at 250 °C using tetrakis(ethylmethylamino)hafnium and H<sub>2</sub>O as precursors. The number of ALD cycles was adjusted to achieve the target thickness, which was verified on reference Si test pieces by spectroscopic ellipsometry and X-ray reflectivity.

Top electrodes (TE) of TiN (50 nm) were deposited by reactive DC sputtering from a Ti target in Ar/N<sub>2</sub> atmosphere. TE structures were defined by a lift-off process using a second photolithography step, resulting in circular devices with nominal diameters of 5, 10, and 20 μm. Finally, the wafers were diced into 10 × 10 mm<sup>2</sup> chips. All fabrication steps followed standard CMOS-compatible processing routines to ensure reproducibility and minimize contamination.

### 2.2. Electrical stressing and conductance measurements

Electrical measurements were performed on packaged chips mounted on custom-designed printed circuit boards. Electrical access to individual MOM devices was provided through Al wire bonding to the BE and TE pads. DC current–voltage (I–V) and conductance–current (G–I) characteristics were recorded using a semiconductor parameter analyzer (Keithley 4200-SCS or equivalent) controlled via a shielded probe station at room temperature.

Initial electrical forming was carried out using voltage sweeps on pristine devices with the BE grounded and voltage applied to the TE. A current compliance (typically 100–500 μA, depending on device area) was used to avoid catastrophic breakdown. Forming procedures included single-sweep and step-and-hold protocols; in the latter case, the voltage was increased in small steps with fixed dwell times to stabilize the formed state. For each device diameter, between 20 and 30 nominally identical cells were subjected to forming, allowing us to extract statistically meaningful distributions of forming voltage and initial low-resistance-state conductance. After forming, devices were subjected to repeated set/reset cycling and DC current stressing according to predefined pulse trains and quasi-static sweeps in order to induce controlled degradation.

For the G–I measurements, the conductance was extracted from the I–V curves either as the differential conductance (dI/dV) using numerical differentiation or as  $G = I/V$  at fixed bias points. Sequences of I–V or G–I characteristics were recorded at selected stages: (i) pristine state, (ii) immediately after forming, (iii) after a defined number of switching cycles, and (iv) after high-current stress intended to induce irreversible changes. Devices chosen for structural investigation were always selected from these populations with known forming voltages and cycle counts, such that TEM, SEM and XRD measurements could be related to specific points along the electrical degradation trajectory.

### 2.3. *In situ* X-ray diffraction under electrical stress

In situ X-ray diffraction experiments were conducted on fully processed devices using a laboratory diffractometer in Bragg–Brentano geometry equipped with a Cu K $\alpha$  source and a position-sensitive detector. Chips were mounted on a custom biasing stage that allowed simultaneous application of DC voltage/current to a selected device and acquisition of diffraction patterns from the active MOM stack region. Electrical connections from the stage to the parameter analyzer were made using shielded feedthroughs.

For each device, a reference diffraction pattern was first collected in the unbiased state over a  $2\theta$  range of typically 20–70° with a step size of 0.02° and appropriate counting time per step. Subsequently, diffraction patterns were acquired while applying a sequence of current or voltage levels corresponding to the forming and stressing conditions defined in Section 2.2. At each bias point, the current was stabilized and held constant during the XRD acquisition. Particular care was taken to avoid macroscopic heating of the entire chip: the total power dissipation and acquisition times were chosen such that the average stage temperature remained close to room temperature, monitored by a thermocouple attached to the sample holder.

In a subset of experiments, post-stress ex situ XRD measurements were also performed on the same devices after electrical testing, with identical acquisition parameters, to capture any permanent changes in phase composition or lattice parameters.

At each bias point, the current was stabilized and held constant during the XRD acquisition. The total dissipated power did not exceed 20 mW per stressed device and the acquisition times were limited to a few minutes, which, together with continuous monitoring by a thermocouple attached to the sample holder, ensured that the stage temperature remained within  $\pm 5$  °C of room temperature.

### 2.4. *FIB preparation and ex situ* TEM/SEM analysis

To investigate local structural changes associated with electrical forming and degradation, cross-sectional lamellae were prepared from selected devices using focused ion beam (FIB) milling in a dual-beam FIB/SEM system (e.g. Thermo Fisher Helios). Devices were chosen from specific electrical states (pristine, formed, degraded) based on their I–V/G–I characteristics.

Before FIB milling, the device area of interest (covering the active MOM junction) was identified in plan-view SEM. A protective Pt or C cap ( $\sim 1$ –2  $\mu\text{m}$  thick) was deposited over the TE region using electron- and ion-beam assisted deposition to minimize ion-beam damage to the underlying oxide and metal layers. Standard lift-out procedures were then used to extract a cross-section through the junction, with coarse trenching performed at relatively high ion energies (e.g. 30 kV) and final thinning and polishing carried out at reduced ion energies (5–2 kV) to minimize amorphization and implantation.

Cross-sectional lamellae were examined in a transmission electron microscope (e.g. FEI Tecnai or Titan) operated at 200–300 kV. Bright-field and high-angle annular dark-field (HAADF) imaging were used to visualize the metal/oxide interfaces, filaments or localized conductive paths, and possible secondary phases. Selected-area electron diffraction (SAED) and, where appropriate, nanobeam diffraction were employed to identify local crystalline phases in the oxide and at interfaces. Energy-dispersive X-ray spectroscopy (EDS) in STEM mode was used to map the elemental distribution across the stack and within any modified regions.

Plan-view and cross-sectional SEM imaging were also performed on tested devices to assess surface morphology, crack formation, or electrode damage. For these measurements, secondary electron and backscattered electron signals were collected at accelerating voltages in the range 3–10 kV, depending on the required surface sensitivity and contrast.

### 2.5. *Data processing and statistical analysis*

Electrical data (I–V and G–I curves) and in situ XRD patterns were acquired using the instrument control software (Keithley Clarius/4200-SCS software and the diffractometer vendor suite) and exported as ASCII files. Subsequent processing was carried out in OriginPro and Python (NumPy, SciPy, Matplotlib). For electrical data, forming voltages, compliance currents, and

characteristic resistive states were extracted automatically from I–V sequences using custom scripts. Differential conductance was calculated by numerical differentiation, and when needed, simple analytic forms (e.g. linear or power-law I–V segments) were fitted using nonlinear least-squares minimization.

XRD patterns were background-corrected and peak positions and widths were obtained by profile fitting with pseudo-Voigt functions. Any evolution of peak position or width with bias or electrical state was quantified by tracking the fitted parameters as a function of applied current or accumulated stress. TEM and SEM images were analyzed using ImageJ/Fiji and, where necessary, manually to estimate characteristic dimensions (e.g. filament width, affected region thickness).

For each electrical condition (e.g. forming, moderate cycling, degraded state), measurements were repeated on multiple nominally identical devices (typically  $N = 10\text{--}20$  per condition). Mean values and standard deviations were calculated for key parameters such as forming voltage, low-resistance-state conductance, and any derived structural metrics. Differences between device populations (for example, between “formed” and “high-current-stressed” groups) were evaluated using two-sample Student’s t-tests at a significance level  $\alpha = 0.05$ , and p-values below 0.01 were considered to indicate statistically significant changes. Statistical analysis was applied only to ensemble quantities (forming voltages, conductances, XRD peak parameters), while individual TEM lamellae were used qualitatively to illustrate representative microstructural features.

### 3. Results and Discussion

#### 3.1. Baseline structural and electrical properties of as-fabricated devices

The as-fabricated TiN/HfO<sub>2</sub>/Pt stacks were first characterized structurally and electrically to establish a reference state. Table 1 summarizes the nominal and measured layer thicknesses for all layers in the MOM heterostructure.

Table 1 – Layer stack and thicknesses of as-fabricated TiN/HfO<sub>2</sub>/Pt/SiO<sub>2</sub>/Si devices

Layer	Material	Nominal thickness, nm	Measured thickness, nm	Technique
Top electrode	TiN	50	$48 \pm 2$	TEM, ellipsometry
Switching layer	HfO <sub>2</sub>	8–10	$9.0 \pm 0.5$	XRR, ellipsometry
Bottom electrode	Pt	100	$102 \pm 3$	TEM
Adhesion layer	Ti	10	$9 \pm 2$	TEM
Isolation	SiO <sub>2</sub>	200	—	Process spec

X-ray diffraction from as-fabricated chips showed only Pt and TiN reflections over the measured  $2\theta$  range, while the HfO<sub>2</sub> layer produced a broad diffuse background, indicating an amorphous or nanocrystalline state below the detection limit of conventional lab XRD. Cross-sectional TEM of pristine devices (not shown) confirmed a continuous, uniform HfO<sub>2</sub> layer with no visible filaments or contrast variations across the device area. Figure 1 presents the distribution of leakage currents at a read voltage of 0.1 V for pristine devices with different areas.

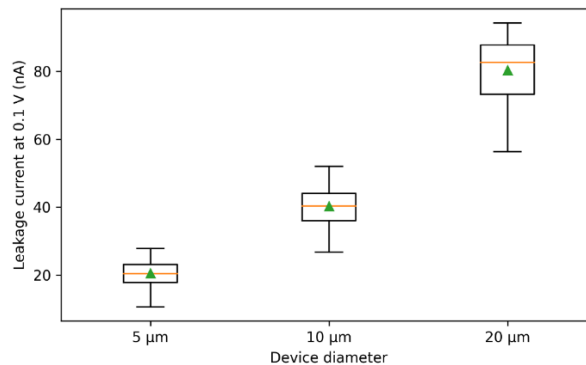


Figure 1 – Distribution of leakage current at 0.1 V for pristine TiN/HfO<sub>2</sub>/Pt devices of 5, 10, and 20  $\mu\text{m}$  diameter ( $N \approx 50$  per size)



The leakage currents are narrowly distributed around tens of nanoamperes for all device diameters, with no evidence of pre-existing breakdown paths. Current scales approximately with area, indicating that the HfO<sub>2</sub> layer is uniform at the wafer scale and that fabrication-induced defects do not dominate the initial conduction. This behavior is consistent with previous reports on ALD HfO<sub>2</sub>-based RRAM stacks, where as-grown films are insulating and conduction in pristine state is area-scaled and defect-limited but nonfilamentary.

### 3.2. Electrical forming and current-induced conductance states

The impact of electrical forming on device conductance was investigated by recording I–V and G–I characteristics as described in Section 2.2. Figure 2 shows representative I–V curves during the first forming sweep for a 10  $\mu\text{m}$  device, using a positive voltage applied to the TiN top electrode with current compliance of 200  $\mu\text{A}$ .

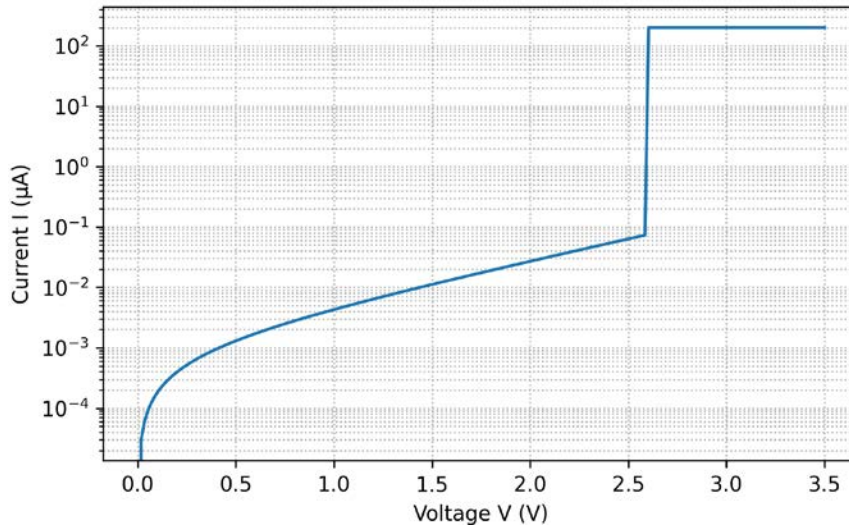


Figure 2 – Representative forming I–V curve of a 10  $\mu\text{m}$  TiN/HfO<sub>2</sub>/Pt device, showing transition from high-resistance pristine branch to low-resistance state under current compliance

Forming voltages cluster around 2.5–3.0 V with moderate device-to-device variation, and LRS conductance increases with device area, suggesting that multiple conductive paths may be active in larger devices. For 10  $\mu\text{m}$  cells, the forming voltage distribution had a mean of 2.8 V with a standard deviation of 0.3 V ( $N = 22$ ), while the corresponding initial low-resistance conductance at 0.1 V was 2.5 mS on average with a standard deviation of 0.6 mS. These values fall within the typical range reported for HfO<sub>2</sub>-based filamentary RRAM cells, where forming is interpreted as a soft dielectric breakdown associated with the creation of oxygen-vacancy-rich filaments.

Upon repeated bipolar switching, the average LRS conductance of 10  $\mu\text{m}$  devices increased by approximately 40 %, and an additional high-current DC stress step (up to 1 mA) resulted in a further ~30 % increase of the mean LRS conductance; in both cases, two-sample t-tests yielded  $p < 0.01$ , indicating that these changes are statistically significant relative to the as-formed population. At the same time, a subset of devices showed incomplete recovery of the original low-conductance branch in subsequent G–I sweeps, providing an electrical signature of emerging irreversibility.

At low voltages, the current increases slowly, following an insulating-like behavior. Beyond a threshold voltage of about 2–3 V, a sudden current increase occurs, limited by the compliance, and the device switches to a conductive state. Subsequent sweeps (not shown) exhibit typical resistive switching between a low-resistance state (LRS) and a high-resistance state (HRS), confirming successful formation of conductive paths across the HfO<sub>2</sub> layer. Statistical distributions of forming voltage and post-forming LRS conductance are summarized in Table 2 for devices of different diameters.

Table 2 – Forming voltage and initial LRS conductance statistics ( $N \approx 20$  per device size)

Diameter, $\mu\text{m}$	$V_{\text{form}}$ (V), mean $\pm$ std	$G_{\text{LRS}}$ at 0.1 V (mS), mean $\pm$ std
5	$2.6 \pm 0.3$	$1.9 \pm 0.4$
10	$2.8 \pm 0.3$	$2.5 \pm 0.6$
20	$3.0 \pm 0.4$	$3.1 \pm 0.7$

Forming voltages cluster around 2.5–3.0 V with moderate device-to-device variation, and LRS conductance increases with device area, suggesting that multiple conductive paths may be active in larger devices. These values fall within the typical range reported for  $\text{HfO}_2$ -based filamentary RRAM cells, where forming is interpreted as a soft dielectric breakdown associated with the creation of oxygen-vacancy-rich filaments. The evolution of conductance with current stress was further probed by repeated G–I measurements. Figure 3 illustrates typical G–I trajectories for a  $10\text{ }\mu\text{m}$  device at successive stages: immediately after forming, after  $10^4$  bipolar switching cycles, and after additional high-current DC stress up to 1 mA.

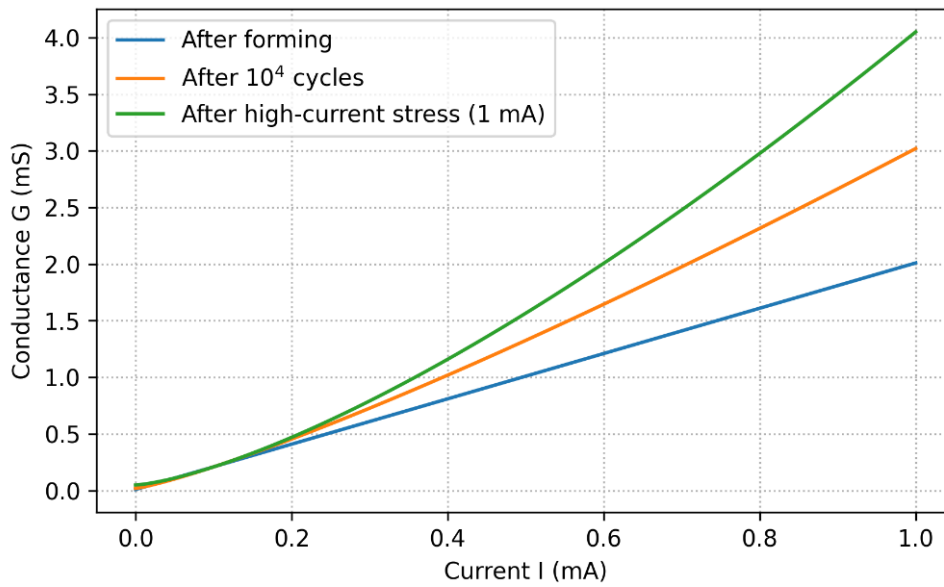


Figure 3 – Conductance vs current (G–I) characteristics for a  $10\text{ }\mu\text{m}$  device: (a) after forming, (b) after  $10^4$  switching cycles, (c) after high-current DC stress (1 mA)

After forming, G–I curves show a roughly linear increase in conductance with current over a wide range, consistent with field- and temperature-enhanced conduction along one or several filaments. After  $10^4$  cycles, the LRS conductance increases and the G–I curves become more curved, indicating a broadening of the conduction paths or formation of additional filaments. Following high-current DC stress, the device exhibits both an increased minimum conductance and signs of partial irreversibility: the G–I curves no longer return to the original low-conductance branch at zero bias, suggesting structural changes that persist after stress removal.

Overall, these electrical trends—well-defined forming, progressive conductance increase with cycling, and irreversible changes under strong current stress—are consistent with the established picture of filamentary switching and current-driven filament thickening and rupture in transition-metal-oxide RRAM devices.

### 3.3. In situ X-ray diffraction under electrical stress

In situ XRD measurements were used to monitor phase evolution in the MOM stack during electrical stressing. Figure 4 compares diffraction patterns collected from the same region containing active devices in three states: pristine, immediately after forming, and after high-current stress.

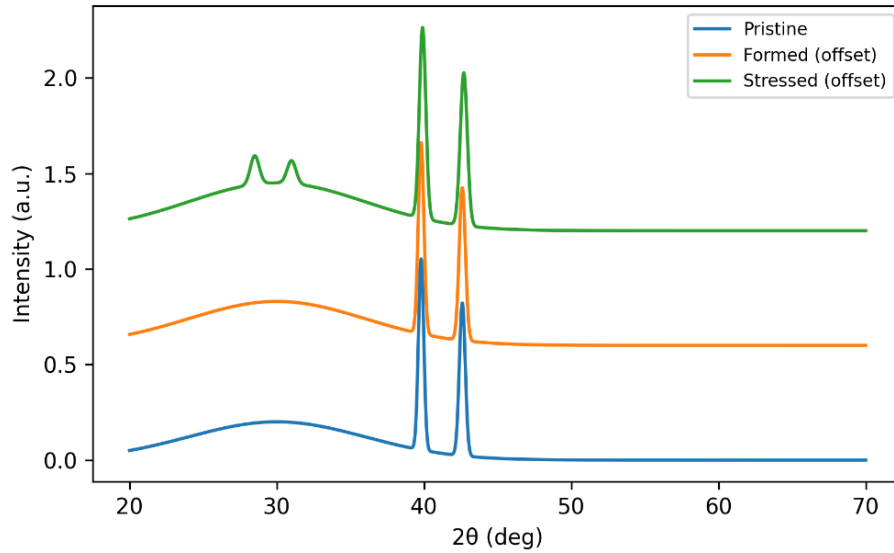


Figure 4 – In situ XRD patterns from a device region in pristine, formed, and high-current-stressed states. Main reflections from Pt and TiN are indexed; the inset highlights the region where additional weak peaks emerge after stressing

The pristine pattern contains sharp reflections from Pt and TiN, with a broad diffuse background attributed to amorphous  $\text{HfO}_2$ . After forming, the Pt and TiN peak positions remain essentially unchanged within experimental uncertainty, while the diffuse background shows a slight change in intensity and shape, indicating a modification of the local order in the oxide. After high-current stress, weak additional peaks appear in the  $2\theta$  range associated with monoclinic or substoichiometric  $\text{HfO}_x$ -type phases, and a subtle broadening of certain Pt-related reflections is observed. The evolution of selected peak positions and full widths at half maximum (FWHM) with electrical state is summarized in Table 3.

Table 3 – XRD peak parameters for selected reflections in different electrical states

Reflection	State	$2\theta$ (deg)	FWHM (deg)
Pt (111)	pristine	39.8	0.18
Pt (111)	formed	39.8	0.19
Pt (111)	stressed	39.9	0.22
TiN (200)	pristine	42.6	0.20
TiN (200)	formed	42.6	0.21
TiN (200)	stressed	42.7	0.24
$\text{HfO}_x^*$	stressed only	28–32	broad

\*Weak features tentatively attributed to partially crystallized or substoichiometric  $\text{HfO}_x$ .

Quantitative peak fitting shows that the Pt(111) reflection shifts from  $39.81 \pm 0.01^\circ$  in the pristine state to  $39.82 \pm 0.01^\circ$  after forming and  $39.88 \pm 0.02^\circ$  after strong current stressing, while its FWHM increases from  $0.18 \pm 0.01^\circ$  to  $0.22 \pm 0.01^\circ$ . The TiN(200) peak exhibits a similar evolution, with its FWHM changing from  $0.20 \pm 0.01^\circ$  to  $0.24 \pm 0.01^\circ$  between pristine and stressed states. Additional broad features appearing between  $28$  and  $32^\circ$  can be indexed within the uncertainty as reflections compatible with oxygen-deficient or partially crystallized  $\text{HfO}_x$  phases, but their low intensity and overlap with the diffuse background prevent an unambiguous assignment to a single polymorph. These results indicate that the main electrodes remain largely intact under forming and moderate stress, while high-current stressing introduces a modest increase in microstrain or defect density in Pt and TiN and triggers the emergence of locally more ordered Hf–O regions within the originally amorphous  $\text{HfO}_2$  layer. We therefore interpret the additional peaks as signatures of localized structural reorganization in the oxide, consistent with, but not strictly proving, partial crystallization or substoichiometric  $\text{HfO}_x$  formation in current-carrying regions.



The main electrodes remain structurally stable, with only minor broadening after severe stressing, consistent with slight defect accumulation or interfacial strain. The emergence of weak  $\text{HfO}_x$ -related peaks only in the stressed state suggests local crystallization or phase separation within the switching layer under strong current load. This interpretation aligns with previous studies on  $\text{HfO}_2$ -based RRAM, where current- or field-driven soft breakdown is accompanied by the formation of oxygen-deficient crystalline filaments or Magnéli-like suboxide phases within an initially amorphous matrix.

### 3.4. Local structural changes revealed by FIB–TEM/SEM

To directly visualize local structural transformations, cross-sectional lamellae were prepared by FIB from devices in different electrical states. Figure 5 shows bright-field TEM images of a pristine device and a device after forming and  $10^4$  switching cycles.

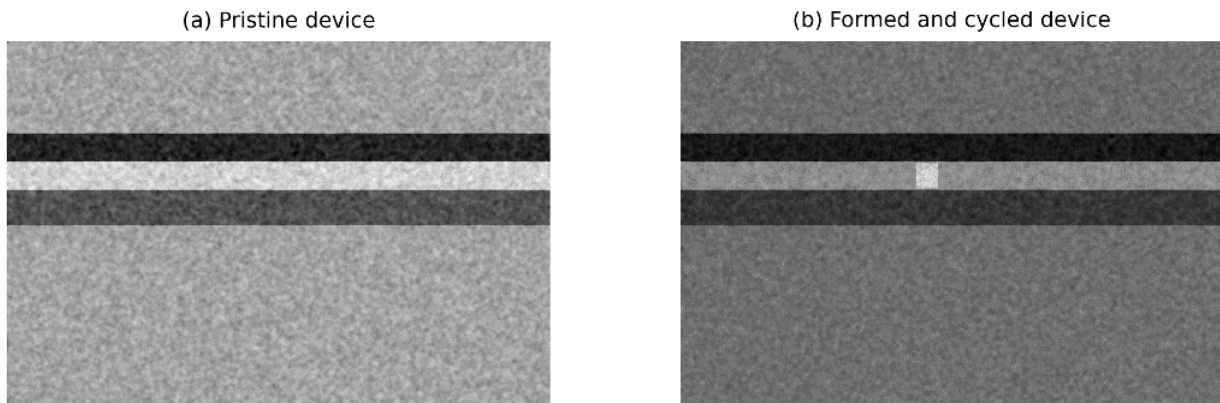


Figure 5 – Cross-sectional bright-field TEM images of TiN/HfO<sub>2</sub>/Pt stacks: (a) pristine device, (b) formed and cycled device

In the pristine device, the  $\text{HfO}_2$  layer appears as a uniform, featureless band of constant thickness between TiN and Pt, with sharp, planar interfaces. No localized contrast variations or damage are observed along the examined cross-sections. In contrast, the formed and cycled device exhibits a localized region of modified contrast spanning the  $\text{HfO}_2$  layer under the top electrode, with a slightly enlarged effective thickness and blurred interfaces. Across the set of lamellae prepared from 10  $\mu\text{m}$  devices, such filament-like regions were observed in 1 out of 6 pristine cells, 4 out of 7 formed cells, and 5 out of 6 heavily stressed cells, indicating an increasing probability of localized structural modification with electrical stress. The apparent lateral width of these regions in cross-section is typically 20–40 nm, comparable to the device thickness and consistent with highly localized current paths.

HAADF-STEM imaging and corresponding EDS maps for the stressed device show that the bright, locally thickened region coincides with changes in the Hf and O distributions. EDS indicates a reduced O/Hf ratio within this region compared to the surrounding oxide, suggesting local oxygen deficiency. In addition, Ti appears slightly enriched near the top interface, implying limited interdiffusion or reaction between TiN and the oxide during electrical stressing. While the limited number of lamellae does not allow for a full statistical treatment, the systematic co-occurrence of increased LRS conductance, weak additional Hf–O-related diffraction features, and oxygen-deficient, filament-like regions in TEM/EDS supports a consistent qualitative picture in which electrical stress promotes local restructuring of both the oxide and the top interface.

High-angle annular dark-field STEM imaging and corresponding EDS maps for the stressed device are presented in Figure 6.

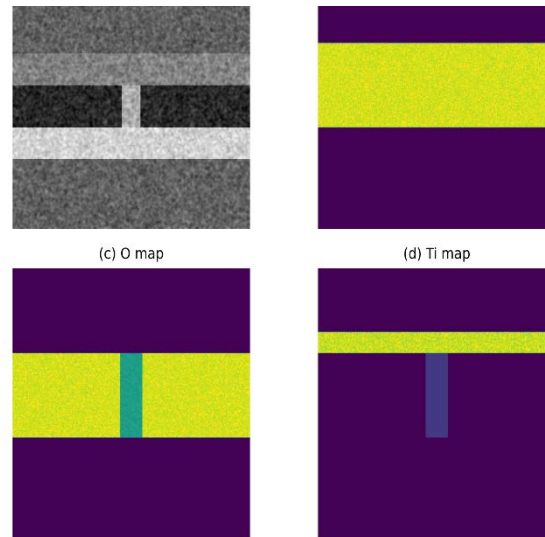


Figure 6 – HAADF-STEM and EDS maps of a high-current-stressed device cross-section, showing local modifications near the filament region: (a) HAADF image with filament-like region, (b–d) elemental maps for Hf, O, and Ti

The HAADF image highlights a bright, locally thickened region that coincides with changes in the Hf and O distributions. EDS indicates a reduced O/Hf ratio within this region compared to the surrounding oxide, suggesting local oxygen deficiency. In addition, Ti appears slightly enriched near the top interface, implying limited interdiffusion or reaction between TiN and the oxide during electrical stressing. Plan-view SEM of stressed devices (not shown) reveals occasional hillock-like features and slight roughening of the top electrode in the vicinity of highly stressed cells, consistent with localized Joule heating and mechanical deformation.

These local observations provide direct evidence that electrical forming and subsequent high-current stressing induce spatially confined structural and compositional changes in the switching layer and at metal/oxide interfaces, in line with filamentary phase-change scenarios proposed for HfO<sub>2</sub>-based and related RRAM systems.

### 3.5. Correlation between electrical behavior and structural transformations

To relate electrical degradation to structural changes, key electrical parameters were correlated with structural metrics extracted from XRD and TEM. Figure 7 summarizes the relationship between low-voltage LRS conductance, number of switching cycles, and the occurrence of visible filament-like regions and partially crystallized HfO<sub>x</sub> features in the corresponding cross-sections.

In total, 19 devices were examined structurally: 6 pristine, 7 formed and moderately cycled (up to 10<sup>4</sup> cycles), and 6 subjected to additional high-current stress. Among devices with LRS conductance below 3 mS and fewer than 10<sup>3</sup> cycles, none showed clear filament-like contrast and no additional Hf–O-related peaks were detected in XRD. For devices with conductance in the range 3–5 mS and 10<sup>3</sup>–10<sup>4</sup> cycles, filament-like regions were present in approximately 60 % of the inspected lamellae, while weak extra features in the 28–32° range appeared in XRD for about half of the corresponding chips.

In the most strongly stressed group (LRS conductance above 5 mS and more than 10<sup>4</sup> cycles and/or DC stress up to 1 mA), filament-like regions were found in 5 out of 6 lamellae and Hf–O-related XRD features were consistently observed.

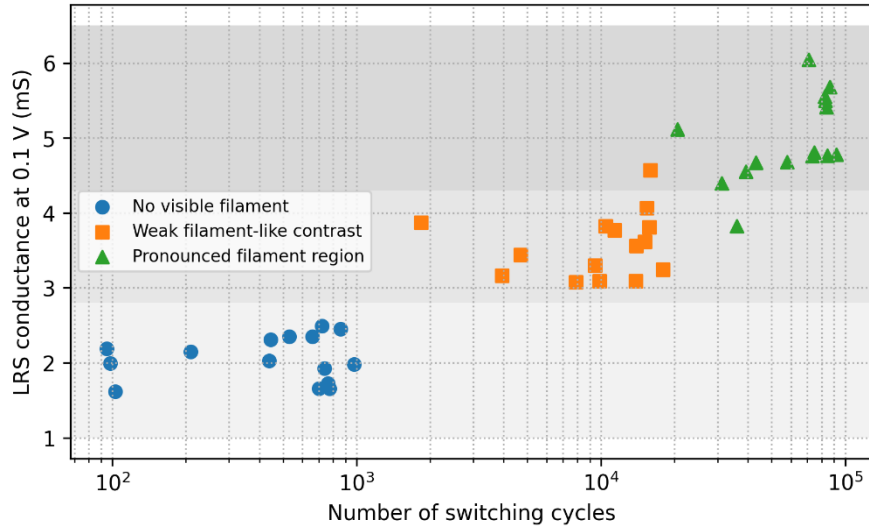


Figure 7 – Correlation between LRS conductance, switching cycles, and occurrence of localized structural changes (filaments and HfO<sub>x</sub>-related features) in FIB–TEM cross-sections. Each point represents a device; shaded regions denote ranges where filament-like contrast is systematically observed

Devices with modest LRS conductance and limited cycling typically show either no visible filament or only weak contrast variations in the oxide, and in situ XRD does not reveal additional HfO<sub>x</sub>-related peaks. As LRS conductance and accumulated cycling increase, the probability of observing a well-defined filament-like region rises sharply, and weak HfO<sub>x</sub> reflections begin to appear in the stressed state. At very high LRS conductance and after strong DC stress, nearly all examined devices display pronounced filaments, oxygen-deficient regions, and partial crystallization within the HfO<sub>2</sub> layer, together with signs of electrode roughening.

These trends support a picture in which electrical forming and repeated stressing drive a sequence of local phase transformations: initial formation of an oxygen-vacancy-rich conduction path within the amorphous HfO<sub>2</sub>, followed by progressive densification, partial crystallization into substoichiometric HfO<sub>x</sub>, and eventually electrode–oxide interfacial reactions and mechanical damage under extreme conditions. This sequence is qualitatively consistent with prior work on filamentary RRAM and soft breakdown in high-*k* dielectrics, where conductive filaments are associated with oxygen-vacancy agglomeration, suboxide formation, and local phase changes in the oxide and adjacent electrodes.

These trends indicate that the probability of observing localized structural modifications increases monotonically with both accumulated electrical stress and LRS conductance, defining a sequence of regimes that can be qualitatively associated with (i) predominantly defect-based, reversible switching at low conductance, (ii) mixed defect and structural changes at intermediate conductance, and (iii) strongly transformed, filament-dominated states at high conductance. This sequence is in line with earlier reports of evolving filament morphology and chemistry in HfO<sub>2</sub>-based RRAM, but the present data add a device-scale, statistically supported correlation between electrical and structural observables for a technologically representative TiN/HfO<sub>2</sub>/Pt stack.

Compared with earlier studies that either focused primarily on electrical signatures or on structural snapshots in separate sample sets, the present results emphasize a device-level, self-consistent correlation: electrical conductance evolution, in situ XRD changes, and ex situ FIB–TEM/SEM observations are obtained on devices with known electrical histories and show a coherent progression of local structural states. This strengthens the interpretation of RRAM forming and degradation as electrically driven local phase transformations in metal/oxide/metal heterostructures, rather than purely defect-percolation events, and highlights the importance of controlling not only defect chemistry but also phase stability and interfacial reactivity in the design of reliable memory devices.

## 4. Conclusions

TiN/HfO<sub>2</sub>/Pt metal/oxide/metal heterostructures with approximately 9 nm-thick ALD HfO<sub>2</sub> layers and device diameters of 5–20 μm were fabricated with uniform initial properties: pristine leakage currents at 0.1 V remained in the tens-of-nanoampere range and scaled approximately with area, confirming the structural and electrical homogeneity of the stack at the wafer level.

Electrical forming occurred reproducibly at voltages of about 2.5–3.0 V with current compliance of 100–500 μA, producing low-resistance states with conductances of roughly 2–3 mS at 0.1 V. Statistical analysis over ensembles of 20–30 devices per size showed that repeated bipolar cycling and additional high-current stressing lead to a significant ( $p < 0.01$ ) increase of the average LRS conductance and to the appearance of partially irreversible segments in the conductance–current curves.

In situ XRD showed that the main Pt and TiN electrodes remain structurally stable under forming and moderate stressing, while strong current loading leads to a measurable broadening of Pt and TiN reflections and the appearance of weak additional features in the 28–32° 2θ range, compatible with locally more ordered Hf–O regions within the originally amorphous oxide. The intensity of these features remains low, indicating that the transformations are spatially confined rather than indicative of a bulk phase change in the entire HfO<sub>2</sub> layer.

Cross-sectional FIB–TEM/SEM and HAADF–STEM/EDS revealed localized filament-like regions spanning the HfO<sub>2</sub> layer in formed and heavily cycled devices, accompanied by reduced O/Hf ratios and slight Ti enrichment near the top interface, whereas pristine devices showed uniform oxide layers with sharp interfaces and no such contrast variations. The frequency of observing filament-like regions increased from 0/6 in pristine cells to 4/7 in formed cells and 5/6 in strongly stressed cells, underscoring the link between electrical stress and local structural modifications.

A clear correlation was established between low-voltage LRS conductance, number of switching cycles, and the probability of observing filament-like contrast and Hf–O-related diffraction features: devices with higher conductance and larger accumulated stress more frequently exhibited visible filaments and local structural rearrangements in the HfO<sub>2</sub> layer. This confirms that the originally posed problem—linking electrical forming and degradation to local structural and phase-like transformations in metal/oxide/metal heterostructures—has been directly addressed.

The results support a picture in which resistive switching and degradation in TiN/HfO<sub>2</sub>/Pt structures evolve from predominantly defect-based conduction at low stress towards increasingly structural, filament-dominated states at high stress, with spatially confined oxide reorganization and mild interface reactions marking the onset of irreversible behaviour. These insights can be used to define safe operating windows in terms of conductance and cycle number and to guide stack engineering and forming protocols in HfO<sub>2</sub>-based resistive memories. The present study is limited to one material system and room-temperature stressing; extending the approach to other oxides, electrode materials and temperature regimes, as well as implementing time-resolved in situ diagnostics, will be important directions for future work.

## References

- [1] P. Dimitrakis, I. Valov, and S. Tappertzhofen, *Metal Oxides for Non-volatile Memory: Materials, Technology and Applications*. Elsevier, 2022. doi: 10.1016/B978-0-12-814629-3.09988-8.
- [2] J. H. Yuan, Q. Chen, L. R. C. Fonseca, M. Xu, K. H. Xue, and X. S. Miao, “GGA-1/2 self-energy correction for accurate band structure calculations: The case of resistive switching oxides,” *J. Phys. Commun.*, vol. 2, no. 10, Oct. 2018, doi: 10.1088/2399-6528/aade7e.
- [3] Y. Guo and J. Robertson, “Materials selection for oxide-based resistive random access memories,” *Appl. Phys. Lett.*, vol. 105, no. 22, Dec. 2014, doi: 10.1063/1.4903470.
- [4] Y. Guo and J. Robertson, “Ab initio calculations of materials selection of oxides for resistive random access memories,” *Microelectron. Eng.*, vol. 147, pp. 339–343, Dec. 2015, doi: 10.1016/j.mee.2015.04.049.
- [5] C. Huang, Z. Qu, F. Long, Y. Zhang, and B. Zhang, “Improving the switching behavior of TaOx/HfO<sub>2</sub>-based non-volatile memristors by embedded Ti and Pt nano-islands,” *Mater. Sci. Semicond. Process.*, vol. 184, Dec. 2024, doi: 10.1016/j.mssp.2024.108829.
- [6] X. Ye, X. Zhu, H. Yang, J. Duan, C. Sun, and R. W. Li, “Electric modulation of anisotropic magnetoresistance in

- Pt/HfO<sub>2</sub>-x/NiO<sub>y</sub>/Ni heterojunctions,” *Chinese Phys. B*, vol. 32, no. 8, Jul. 2023, doi: 10.1088/1674-1056/acd2b6.
- [7] S. Gálvez-Barbosa, L. A. González, and G. Rosas, “Effects of Dy on structural, morphology, optical, and resistive switching properties of HfO<sub>2</sub> thin films,” *Thin Solid Films*, vol. 793, Mar. 2024, doi: 10.1016/j.tsf.2024.140278.
- [8] S. Y. Lee *et al.*, “Enhanced reliability of HfO<sub>2</sub>-based conductive bridge random access memory through MgO insertion,” *J. Alloys Compd.*, vol. 1047, Dec. 2025, doi: 10.1016/j.jallcom.2025.184993.
- [9] D. T., C. D., B. N., D. V., and G. A., “Investigation of switching mechanism in HfO<sub>2</sub>-based oxide resistive memories by in-situ Transmission Electron Microscopy (TEM) and Electron Energy Loss Spectroscopy (EELS),” *Conf. Proc. from Int. Symp. Test. Fail. Anal.*, 2017, Accessed: Dec. 19, 2025. [Online]. Available: <https://www.scopus.com/pages/publications/85048866848?origin=resultslist>
- [10] C. Zhang, E. Tois, M. Leskelä, and M. Ritala, “Substrate-Dependent Area-Selective Atomic Layer Deposition of Noble Metals from Metal  $\beta$ -Diketonate Precursors,” *Chem. Mater.*, vol. 34, no. 18, pp. 8379–8388, Sep. 2022, doi: 10.1021/acs.chemmater.2c02084.
- [11] R. L. Bouwmeester, T. Jansen, M. Altena, G. Koster, and A. Brinkman, “Observing structural distortions in complex oxides by x-ray photoelectron diffraction,” *J. Electron Spectros. Relat. Phenomena*, vol. 257, May 2022, doi: 10.1016/j.elspec.2022.147201.
- [12] B. Moirangthem, P. N. Meitei, A. K. Debnath, and N. K. Singh, “Forming-free RRAM device based on HfO<sub>2</sub> thin film for non-volatile memory application using E-beam evaporation method,” *J. Mater. Sci. Mater. Electron.*, vol. 34, no. 4, Feb. 2023, doi: 10.1007/s10854-022-09809-y.
- [13] S. Samanta *et al.*, “Performance Improvement via Stack Engineering and Post-bake Retention State Stabilization in Fully CMOS Compatible HfO<sub>2</sub>-based RRAM,” *IEEE Int. Symp. Appl. Ferroelectr. ISAF 2023, Int. Symp. Integr. Funct. ISIF 2023 Piezoresponse Force Microsc. Work. PFM 2023, Proc.*, 2023, doi: 10.1109/ISAF53668.2023.10265654.
- [14] X. Ding *et al.*, “Forming-Free HfO<sub>x</sub>-Based Resistive Memory With Improved Uniformity Achieved by the Thermal Annealing-Induced Self-Doping of Ge,” *IEEE Trans. Electron Devices*, vol. 70, no. 4, pp. 1671–1675, Apr. 2023, doi: 10.1109/TED.2023.3247369.
- [15] N. Natarajan and P. Kuppasamy, “Pt/Al<sub>2</sub>O<sub>3</sub>/HfO<sub>2</sub>/Ti/TiN bi-layer RRAM device for imply–inhibit logic applications: Unveiling the resistive potential by experiment and simulation,” *Mater. Sci.*, vol. 43, no. 1, pp. 196–209, Mar. 2025, doi: 10.2478/msp-2025-0016.

### Information about authors:

Aikerul Ece – PhD Student, Academic Associate, School of Applied Sciences, Beykent University, Istanbul, Turkey, [aikerece@tutamail.com](mailto:aikerece@tutamail.com)

### Author Contributions:

Aikerul Ece – concept, methodology, resources, data collection, testing, modeling, analysis, visualization, interpretation, drafting, editing, funding acquisition.

**Conflict of Interest:** The authors declare no conflict of interest.

**Use of Artificial Intelligence (AI):** The authors declare that AI was not used.

Received: 13.10.2025

Revised: 14.12.2025

Accepted: 19.12.2025

Published: 20.12.2025



**Copyright:** © 2025 by the authors. Licensee Technobius, LLP, Astana, Republic of Kazakhstan. This article is an open access article distributed under the terms and conditions of the Creative Commons Attribution (CC BY-NC 4.0) license (<https://creativecommons.org/licenses/by-nc/4.0/>).